



Nanoscale

Role of the ZnO Electron Transport Layer in PbS Colloidal Quantum Dot Solar Cell Yield

Journal:	<i>Nanoscale</i>
Manuscript ID	NR-REV-12-2023-006558.R1
Article Type:	Review Article
Date Submitted by the Author:	16-Mar-2024
Complete List of Authors:	<p>Chiu, Arlene; Johns Hopkins University, Electrical and Computer Engineering</p> <p>Lu, Chengchangfeng; Johns Hopkins University, Electrical and Computer Engineering</p> <p>Kachman, Dana; Johns Hopkins University, Electrical and Computer Engineering</p> <p>Rong, Eric; Johns Hopkins University, Electrical and Computer Engineering</p> <p>Chintapalli, Sreyas; Johns Hopkins University, Electrical and Computer Engineering</p> <p>Lin, Yida; Johns Hopkins University, Electrical and Computer Engineering</p> <p>Khurgin, Daniel; Johns Hopkins University, Electrical and Computer Engineering</p> <p>Thon, Susanna; Johns Hopkins University, Electrical and Computer Engineering; Johns Hopkins University, Department of Materials Science and Engineering</p>

SCHOLARONE™
Manuscripts

Journal Name

ARTICLE TYPE

Cite this: DOI:00.0000/xxxxxxxxxx

Role of the ZnO Electron Transport Layer in PbS Colloidal Quantum Dot Solar Cell Yield

Arlene Chiu‡, Chengchangfeng Lu‡, Dana E. Kachman‡, Eric Rong, Sreyas Chintapalli, Yida Lin, Daniel Khurgin, and Susanna M. Thon^a

Received Date

Accepted Date

DOI:00.0000/xxxxxxxxxx

The development of lead sulfide (PbS) colloidal quantum dot (CQD) solar cells has led to significant power conversion efficiency (PCE) improvements in recent years, with record efficiencies now over 15%. Many of the recent advances in improving PCE have focused on improving the interface between the PbS CQD active layer and the zinc oxide (ZnO) electron transport layer (ETL). Proper optimization of the ZnO ETL also increases yield, or the percentage of functioning devices per fabrication run. Simultaneous improvements in both PCE and yield will be critical as the field approaches commercialization. This review highlights recent advances in the synthesis of ZnO ETLs and discusses the impact and critical role of ZnO synthesis conditions on the PCE and yield of PbS CQD solar cells.

1 Introduction

With rising global interest in and demand for sustainable energy, new solar cell technologies are attracting continuing interest. Silicon-based, first generation solar cells are the most widely used due to their high efficiencies and developed supply chain. As silicon solar cell technology has advanced, there has also been significant decreases in the monetary cost, making them competitive as an energy source. However, researchers have continued interest in expanding the applications for solar energy harvesting technology as the limitations of silicon become evident. Specifically, the high temperature purification process for silicon, requiring temperatures as high as 650°C¹, leads to a high energy cost in the manufacturing process, and silicon cells require bulky, rigid, and heavy mounting frames. Second generation solar cells lower the amount of material required by using thin films of direct bandgap semiconductors such as cadmium telluride (CdTe) and copper indium gallium di-selenide (CIGS) as the absorbing layer of the device. Third generation solar cells consist of emerging technologies that are in their commercial infancy. One such technology is colloidal quantum dot (CQD) solar cells. The low temperature and low cost synthesis methods, as well as the solution-processable nature of CQDs, offers advantages for roll-to-roll or spray-casting manufacturing at a large scale onto a variety of flexible substrates²⁻⁵. Lead sulfide (PbS) CQDs are of particular interest, given that the bandgap of this materials system can be

tuned based on the physical size of the CQD to absorb a wide range of the sun's visible and infrared spectrum⁶⁻¹⁰, making them of interest for multi-junction technologies.

Because PbS CQD optoelectronics is an emerging field, most research focuses on methods to improve the device efficiencies. Often, minimal data is reported on the experimental yield, which becomes a critical factor when considering large scale production. By yield, we specifically refer to the percentage of working devices that result from any specific fabrication run, whereby the most common indicators of failure are persistent short circuit or open circuit behavior. Although underreported, the field has faced issues with reproducibility of high-performing PbS CQD solar cells, and these limitations can potentially be attributed to physical defects in the zinc oxide (ZnO) electron transport layer (ETL), leading to persistent short circuits in many solar cells.

Solution-processed ZnO films are currently used as the ETL in the highest efficiency PbS CQD solar cells, as illustrated in the cross-sectional scanning electron microscopy (SEM) image in Figure 1(c) and the corresponding device diagram shown in Figure 1(d). ZnO is an attractive ETL material due to its optical transparency, electron affinity alignment with 1.3 eV bandgap PbS CQD films, and high electron mobility¹¹⁻¹⁴. However, in our work, we discovered that the ZnO layer plays a large factor in experimental yields and repeatability. We often observed varying performances across a single batch of devices made from the same ZnO nanoparticle (NP) solution, with many devices exhibiting low efficiencies or short circuit behavior. We thus undertook a comprehensive review of the recent advancements in ZnO ETLs for PbS CQD solar cells with a focus on both PCE and yield to highlight the current status and future research needs for ZnO

Department of Electrical and Computer Engineering, Johns Hopkins University, 3400 North Charles Street, Baltimore, Maryland, 21218, United States

^a Department of Materials Science and Engineering, Johns Hopkins University, 3400 North Charles Street, Baltimore, Maryland, 21218, United States

‡These authors contributed equally to this work.

ETLs in high performance CQD solar cells.

The base recipes for the sol-gel ZnO used in most PbS CQD solar cells find their origins from Womelsdorf, Hoheisel and Passing¹⁷. Bashir et al. recently proposed a low-temperature synthesis method that allows stable ZnO NPs to be synthesized in less time¹⁸. These alternate methods have yet to gain the same common usage as the Womelsdorf, Hoheisel and Passing method, but may gain popularity in the coming years as the field looks towards improved ETL materials for PbS CQD solar cells¹⁸. This method, illustrated in 1(a), is carried out as follows: first, zinc acetate (ZnAc) dissolved in alcohol undergoes hydrolysis through addition of a base at room temperature or the boiling point of the solution. This produces a whitish precipitate. After allowing the precipitate to settle, additional washing steps can be optionally performed. After washing, the precipitate is redispersed in a final solvent. The resulting ZnO solution can then be deposited on the substrate, typically via spin-casting, and lastly is dried/annealed to remove excess solvent.

Here, we describe the evolution of ZnO synthetic recipes used for the highest performing PbS CQD solar cells, looking at the effects of $\text{Zn}^{2+}:\text{OH}^-$ ratio and a variety of dispersion solvents and additives, as well as investigate the benefits of various surface passivation techniques currently being explored by the field. Additionally, we present the results of experimental work to illustrate the importance of ZnO synthesis parameters in determining both the yield and PCE of PbS CQD solar cells.

2 Development of the Electron Transport Layer in PbS CQD Solar Cells

2.1 Origins and Background

It was first reported in 2005 that spin-cast PbS CQDs produced a photovoltaic response¹⁹. In 2007, a working PbS CQD solar cell with a Schottky junction architecture was demonstrated with an infrared power conversion efficiency (PCE) of 1.3%²⁰. In 2010, the depleted heterojunction architecture²¹ was introduced, based on p-n photovoltaic devices that incorporated an n-type charge transport layer and p-type PbS CQD film with organic ligands. The addition of an ETL allows for photogenerated electrons to be more efficiently extracted, and also serves to block hole transport from the active layer to the cathode, minimizing the non-radiative electron-hole recombination. The idea to use ZnO as an ETL was inspired by the field of organic/hybrid²² and dye-sensitized solar cells²³, which now predominately use organic ETLs and TiO_2 ETLs, respectively. Both ZnO NPs and mesoporous TiO_2 were initially used as the ETL for PbS CQD solar cells, with ZnO ETL devices achieving 3% PCE²⁴ and TiO_2 achieving 3.5 %²⁵ in 2010.

TiO_2 was the dominant ETL for PbS CQD solar cells based on the first iterations of depleted heterojunction architectures that utilized p-type CQD films with organic ligands. ZnO became the ETL of choice for high-performing PbS CQD solar cells as new, primarily halogen-based inorganic ligand strategies for CQDs emerged that were more compatible with ZnO. This change was accompanied by a shift to p-i-n device structures, with the introduction of a p-type hole transport layer (HTL) primarily based on PbS CQD films with ethanedithiol ligands to compliment the

close-to-intrinsic PbS CQD absorbing layer that used primarily inorganic ligands.²⁶ The major change from the ZnO used in 2010 by Nozik et al.²⁴ and in 2011 by Beard et al.²⁷ to the ZnO used by Bawendi et al.²⁶ in 2014 was the precursor concentration and solvent ratios, as summarized in Table 1. It has been shown that the rate of ZnO particle growth and size is dependent on the concentration of precursors and the solution composition^{28,29} and affects the ZnO nanoparticle morphology as well as the ZnO bandgap^{30,31}. The $\text{ZnAc}\cdot 2\text{H}_2\text{O}:\text{KOH}$ ratios used by Bawendi et al.²⁶ have become widely adopted by the field, with advances mainly revolving around different final solvents and solvent ratios. In 2019, 2-methoxyethanol (2MEA) was used as a precursor solvent by Baek et al.³² instead of the MeOH that was popularized by Bawendi et al.²⁶. Currently, MeOH is still the more dominant precursor solvent, but this could be attributed to the 2MEA method being newer and the field not yet having widely adopted it. In more recent years, there has also been the exploration of different additives and methods to passivate surface trap states and improve band alignment; again, the field has yet to adopt a standard additive for the ZnO ETL.

2.2 Solvent Engineering

The initial dispersion solvent used for the ZnO nanoparticle solution was chloroform (CF)⁵⁶. In 2016 Lan et al.³⁵ added methanol (MeOH) and dispersed the ZnO nanoparticles in a CF:MeOH mixture at a 1:1 ratio. This development can be traced to 2014 when Li et al.⁵⁷ studied the effects of solvent-induced nanoparticle agglomeration on the ZnO ETL in organic solar cells (OSCs) which generally use similar ZnO synthesis parameters as the PbS CQD field. They found the optimum ratio, which led to the smallest amount of agglomeration, was 1:1 for CF:MeOH. The 1:1 volume ratio resulted in a transparent solution while higher ratios lead to cloudiness indicating nanoparticle agglomeration and, ultimately, an increase in surface roughness of the films, as seen in Figure 2a-h. This 1:1 ratio is now widely adopted for the ZnO dispersion solvent. More recently, Kumara et al.⁵⁸ performed a similar study, specifically for PbS CQD solar cells, varying the ratio of CF:MeOH and observed that with increasing CF volume in the solution from (1:1) to (2:1), they saw an increase in PCE from 1.07% to 2.94%. Increasing the CF beyond (2:1) led to a decrease in performance. They hypothesized that the (2:1) ratio had the best performance due to the roughness of the resulting ZnO film and the nanocrystal size being on the same order as the PbS CQD size, allowing the CQDs to better fill in the ZnO surface profile, leading to improved junction interface contact.

In addition to the solvent ratios, various additives to the ZnO solution have been used to affect the amount of agglomeration, transparency, and stability, and thereby film quality⁵⁹. The most popularly used additive is ethanolamine (2-aminoethanol, monoethanolamine, ETA, or MEA), a stabilizer base, which reduces agglomeration in the solution phase through the amine functional group and promotes higher thin film quality^{60,61}. Thin films deposited with MEA are of higher crystalline quality,⁶² and more homogeneous and smooth⁶³. There has also been evidence that MEA improves ZnO nanoparticle passivation and reduces pinhole

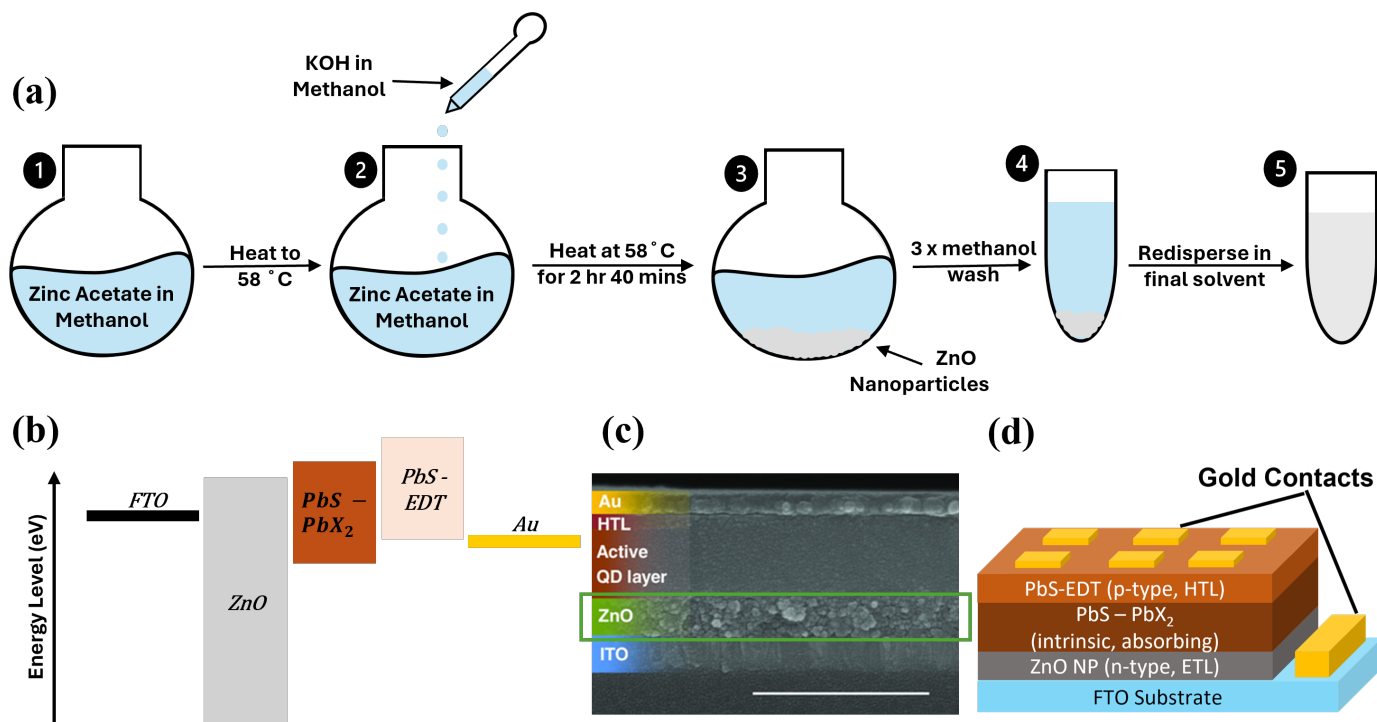


Fig. 1 (a) Schematic of the general process used to synthesize the ZnO NP solution which is used to form the ETL in PbS CQD solar cells. Heating times and temperatures vary across literature. (b) Example band diagram for a PbS CQD solar cell. PbS-PbX₂ refers to a film of PbS CQDs with halide ligands and PbS-EDT refers to a film of PbS CQDs with ethanedithiol ligands prepared using standard procedures¹⁵ (c) Cross sectional SEM micrograph of an example PbS CQD solar cell, with a green box added to indicate the ZnO NP ETL. (c) reproduced with permission from Ref.¹⁶. Copyright 2022, Wiley Online Library. (d) Device schematic for a PbS CQD solar cell.

Table 1 Summary of ZnO Synthesis Methods and Performance

Device Architecture	PCE (%)	Zn Precursor/ Solvent	Base Precursor/ Solvent	Zn ²⁺ :OH ⁻ Ratio	Final Solvent	Heating Temp./Time	Additives	Published Year [Ref.]
ITO/ZnO/PbS-EDT/Au	2.94	ZnAc/MeOH	KOH/MeOH	1:2.3	CF	60C/2hr	-	2010 ²⁴
ITO/ZnO/PbS/TMO/Au	2.66	ZnAc/MeOH	KOH/MeOH	1:2.3	CF	60C/2hr	-	2011 ²⁷
ITO/ZnO/PbS-TBAI/PbS-EDT/Au	8.55	ZnAc•2H ₂ O/MeOH	KOH/MeOH	1:1.7	CF	60C/2.5hr	-	2014 ²⁶
ITO/ZnO-WPF-6-oxy-F/PbS/MoOx/Ag	9.01	ZnAc•2H ₂ O/DMSO	TMAH/ETH	.5M/.1M	IPA	heated/2 hr	WPF-6-oxy-F	2016 ³⁴
ITO/ZnO/PbS-I/PbS-EDT/(MoOx/metal)	9.60	ZnAc•2H ₂ O/MeOH	KOH/MeOH	1:1.7	CF	60C/2.25hr	-	2016 ³³
ITO/ZnO/PbS-TBAI/PbS-EDT/Au	10.18	ZnAc•2H ₂ O/MeOH	KOH/MeOH	1:1.7	CF:MeOH	60 C/2.5 hr	-	2016 ³⁵
ITO/ZnO-EDT/PbS/Au	10.26	ZnAc/DMSO	TMAH/ETH	.5M/.1M	ETH	heated/2hr	EDT	2016 ³⁶
ITO/ZnO/PbS(MAI)-TBAI/PbS-EDT/Au	10.60	ZnAc•2H ₂ O/MeOH	KOH/MeOH	1:1.7	CF:MeOH	RT/2.5hr	-	2016 ³⁷
ITO/ZnO/PbS-TBAI/PbS-EDT/GD/Au	10.64	ZnAc/MeOH & H ₂ O	KOH/MeOH	1:1.7	CF	60C/2.25hr	-	2016 ³⁸
ITO/ZnO/PbS-PbX ₂ /PbS-EDT/Au	11.28	ZnAc•2H ₂ O/MeOH	KOH/MeOH	1:1.7	CF	60/2.5hr	-	2016 ³⁹
ITO/ZnOPbS-EMIL/PbS-EDT/Au	10.47	ZnAc•2H ₂ O/MeOH	KOH/MeOH	1:1.7	CF:1% BTA	60C/2.25hr	-	2017 ⁴⁰
ITO/ZnO/mixed PbS/PbS-EDT/Au	10.4	ZnAc•2H ₂ O & Mg(NO ₃) ₂ •6H ₂ O/ETH	KOH/MeOH	1:1.7	CF:MeOH	60C/2.5hr	-	2017 ⁴¹
ITO/MgZnO/PbS-TBAI/PbS-EDT/Au	10.40	ZnAc•2H ₂ O/MeOH	ethanolamine	-	ETH:MEA	80C/3hr	Mg	2017 ⁴²
ITO/Cl-ZnO/PbS/PbS-EDT/Au	11.6	ZnAc•2H ₂ O/MeOH	KOH/MeOH	1:1.7	CF:MeOH	60C/2.5hr	Cl	2017 ⁴³
ITO/ZnO/PbS-PbX ₂ /PbS-EDT/Au	11	ZnAc•2H ₂ O/MeOH	KOH/MeOH	1:1.7	CF	60C/2.5hr	-	2017 ⁴⁴
ITO/ZnO/PbS-TBAI/PbS-EDT/Au	10.82	ZnAc•2H ₂ O/MeOH	KOH/MeOH	1:1.7	CF	63C/3hr	-	2018 ⁴⁵
ITO/ZnO/PbS-TBAI/PbS-EDT/Au	10.66	ZnAc•2H ₂ O/MeOH	KOH/MeOH	1:1.7	CF	63.5C/3hr	-	2018 ⁴⁶
ITO/ZnMgO/PbS/Au	10.60	ZnAc & MgAc/2ME	-	-	2ME	-	Mg	2019 ⁴⁷
ITO/ZnO/PbS-PbI ₂ /PbS-EDT/Au	11.18	ZnAc•2H ₂ O/MeOH	KOH/MeOH	1:1.7	CF:MeOH	60C/3hr	-	2018 ⁴⁸
ITO/ZnO/PbS-PbX ₂ /PbS-EDT/Au	12.48	ZnAc•2H ₂ O/MeOH	KOH/MeOH	1:1.7	CF:MeOH	60C/2.5hr	-	2018 ⁴⁹
ITO/ZnO/PbS-PbI ₂ /PbS-EDT/Au	11.18	ZnAc•2H ₂ O/MeOH	KOH/MeOH	1:1.7	CF	63C/3hr	-	2019 ⁴⁸
ITO/ZnO/PbS-PbX ₂ /Polymer-SM Bridge/MoO ₂ /Ag	13.1	ZnAc•2H ₂ O/MEA & 2ME	-	-	2ME & MEA	-	-	2019 ³²
FTO/ZnO/PbS-MACI/PbS-EDT/Au	12.40	ZnAc•2H ₂ O/MeOH	KOH/MeOH	1:1.7	CF:MeOH	63.5C/3hr	-	2020 ⁵⁰
ITO/ZnO/PbS-PbX ₂ /Polymer HTL/MoO ₂ /Ag	13.2	ZnAc•2H ₂ O/MeOH	KOH/MeOH	1:1.7	CF	60C/2.5hr	-	2020 ⁵¹
ITO/ZnO/PbS-PbX ₂ & PbS-CTA/PbS-EDT/Au	13.3	ZnAc•2H ₂ O/MeOH	KOH/MeOH	1:1.7	CF	60C/2.5hr	-	2020 ⁵²
ITO/ZnO/PbS-PbX ₂ /Polymer HTL/MoO ₂ /Ag	13.2	ZnAc•2H ₂ O/MeOH	KOH/MeOH	1:1.7	CF	60C/2.5hr	-	2020 ⁵³
ITO/IZO/PbS-EMIL/PbS-EDT/Au	11.1	ZnAc•2H ₂ O & InCl ₃ /MEA & 2ME	-	-	2ME	RT/24hr	In	2021 ⁵⁴
ITO/ZnO/PbX ₂ /PbS-EDT/Au	12.22	ZnAc•2H ₂ O/MeOH	KOH/MeOH	1:1.7	CF	60C/2.5hr	-	2021 ⁵⁵

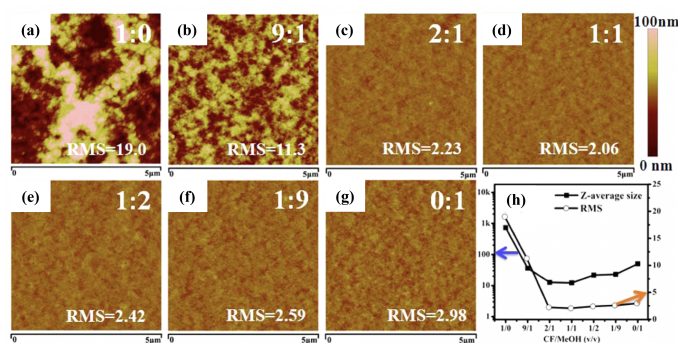


Fig. 2 (a)-(g) Atomic Force Microscopy (AFM) images of ZnO films made from NP solutions with varying CF:MeOH (v:v) ratios. (h) Comparing aggregation variation in ZnO NP thin films and RMS roughness variation of ZnO thin films. Reproduced with permission from Ref. ⁵⁷ Copyright 2014, ACS Publications.

formation in the film phase.⁶⁴

3 Recent Work on Improving ETL Performance in PbS CQD Solar Cells

Beyond agglomeration and physical film quality, it has been documented that the surface states associated with ZnO NPs are sensitive to adsorbates due to the large surface-to-volume ratio⁶⁵, leading to various intrinsic defects, such as oxygen vacancies, Zn interstitials, oxygen interstitials, Zn vacancies.⁶⁶⁻⁷¹ The main surface defects in ZnO can be attributed to oxygen vacancies⁷². It has been shown that these defects can lead to charge carrier accumulation at the ZnO/CQD interface, enhancing the electric field of the device⁷³. Additionally, the conduction band (CB) of ZnO does not align well with the CB of PbX₂-PbS CQDs (X = I, Br), which have been widely adopted as the absorbing layer in high performing PbS CQD solar cells, leading to inefficient charge extraction and increased interfacial recombination⁷⁴⁻⁷⁶. This has led to the investigation of methods for reducing surface defects such as the introduction of interlayers^{33,77,78} and organic polymers⁷⁹. Methods to introduce dopants have been used to address the band alignment issue^{42,47}, and passivation techniques have also been introduced to simultaneously address both issues^{33,36,43}. Here we discuss several methods that have notably improved PbS CQD solar cell efficiencies in further detail.

3.1 ETL Interlayers

One popular approach to improve device efficiencies involves introducing an interlayer between the ZnO ETL and the CQD layer. Azim et al. added a thin layer of poly(9,9-bis((6'-(N,N,N-trimethylammonium)hexyl)-2,7-fluorene)-alt-(9,9-bis(2-(2-(2-methoxyethoxy)ethoxy)ethyl)-9-fluorene)) dibromide (WPF-6-oxy-F) on top of their ZnO layer, creating a WPF-6-oxy-F-modified ZnO and saw an improvement in PCE from 7.14% to 9.01%³³. They found that the addition of WPF-6-oxy-F allowed for better band alignment, shifting the ZnO work function \approx 0.2 eV higher, measured using ultraviolet photoelectron spectroscopy (UPS), as shown in Figure 3b-c. WPF-6-oxy-F also reduced charge recombination as a result of

lower surface defect density, which was characterized using photoluminescence (PL) spectroscopy (Figure 3a). The broad peak in the visible region (\approx 545nm) of the PL is due to defect-related emission^{65,72}. With the suppression of the peak at 545 nm with WPF-6-oxy-F modification (Figure 3a), it can be concluded that there is a reduction in surface defect density. Further, the ethylene oxide (EO) in WPF-6-oxy-F coordinated with the oxygen-vacancies in the ZnO film surface, passivating the surface traps (Figure 3d).

Azim et al., also developed a second method to passivate surface defects via introducing 1,2-ethanedithiol (EDT) (Figure 3h). The EDT ligands passivated the oxygen defects and suppressed interband trap sites (Figure 3e-f), improving the solar cell efficiency from 9.45% to 10.26%³⁶. A change in work function was also noted from 3.68 eV in pristine ZnO to 4.28 eV in EDT treated ZnO (Figure 3g).

3.2 ZnO Passivation

In addition to the use of interlayers, chemical strategies have been demonstrated as an effective route to passivate traps in ZnO and produce better band alignment with the PbS CQD film. One popular method of passivation is the introduction of a variety of ions into the ZnO films. Common choices include chlorine, magnesium, sodium, potassium, and cesium⁸⁰. These ions are expected to fill the oxygen vacancies and reduce the absorbed oxygen on the ZnO NP surfaces, both of which should reduce the density of trap state energy levels within the ETL⁸¹. Furthermore, these passivating ions will have different electronegativities compared to the oxygen in the ZnO lattice, leading to the introduction of larger dipoles, and resulting in band shifts that can contribute to more favorable band alignment⁸¹. Filled trap states are also expected to up-shift the Fermi level, further improving band alignment in PbS CQD solar cells based on ion-passivated ZnO ETLs⁸⁰. As the passivating ions fill oxygen vacancies, the conductivity of the films are expected to improve as well. Fang et al. demonstrated this effect in cesium-doped ZnO NP films by showing that, at low concentration, the introduction of cesium into the ZnO simultaneously reduced the defects in the film and increased the conductivity⁸². At high cesium concentrations, conductivity decreases due to disruption of the ZnO lattice structure⁸².

To highlight the impact of passivation on both ZnO ETL properties and overall device performance, we now describe a few recent advances achieved using these methods. In 2017, Choi et al. developed a method based on chlorine passivation for ZnO NPs, improving PCE from 10.6% to 11.6%⁴³. By adding chlorine (Cl) salts to the solution comprised of ZnO NPs dispersed in MeOH and CF, the surface trap density was reduced, verified using PL measurements (Figure 4a). Using UPS, a shift in the ZnO Fermi energy from 3.02 eV without Cl passivation to 3.30 eV with Cl passivation was observed (Figure 4c). Figure 4d shows the band alignment obtained from UPS and optical measurements. Figure 4d illustrates how the deeper electron affinity allows for better electron extraction.

More recently, Wei et al. extended the idea of Choi et al. by simultaneously using chlorine and sodium ions (Cl⁻¹ and Na⁺¹,

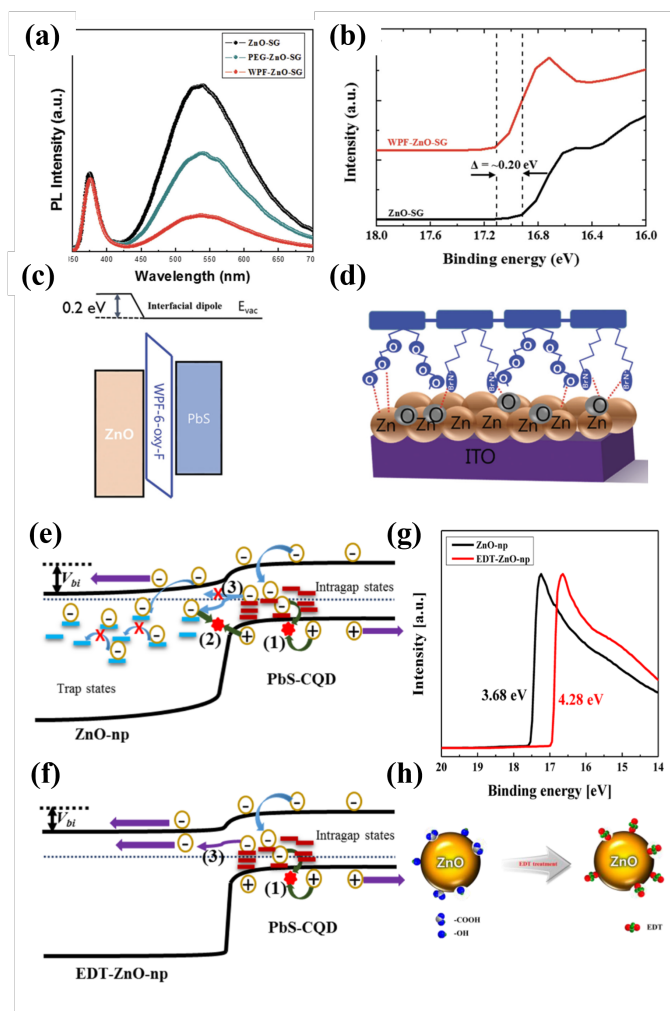


Fig. 3 a) Normalized PL spectra of a ZnO film with and without WPF-6-oxy-F. b) UPS analysis results of the cut-off region for a ZnO film with and without WPF-6-oxy-F. c) Schematic of band bending at the CQD/ZnO heterojunction interface with the addition of a WPF-6-oxy-F interlayer. d) Schematic of a WPF-6-oxy-F interlayer on a ZnO film. (a-d) Reproduced with permission from Ref.³³ Copyright 2016, Wiley Online Library. e) Illustration of charge transport in a pristine ZnO layer and f) an EDT-treated ZnO layer. Process 1 shows bimolecular recombination during charge sweep-out. Process 2 shows interfacial bimolecular recombination induced by trapped charges. Process 3 shows improved extraction of charges through a new intragap band formed by defect reduction. g) UPS of ZnO layers for pristine and EDT-treated films. h) Schematic of surface defect passivation of ZnO via EDT-treatment. (e-h) Reproduced with permission from Ref.³⁶ Copyright 2016, ACS Publications.

respectively) to passivate defects in the ZnO NPs in the solution-phase⁸⁰. Using this approach, they were able to achieve PCE improvements from 7.28% in a conventional device to 9.15% in the NaCl-treated ZnO NP device. They primarily saw improvements in the short-circuit current density (J_{sc}) of their devices, with an improved J_{sc} of 28.6 mA/cm² compared to a J_{sc} of 22.5 mA/cm² in their control devices. Wei et al. propose that the Na⁺ and Cl⁻ fill the oxygen vacancies in the ZnO, reducing the trap-assisted recombination. This result was verified using PL spectroscopy, where a much lower PL signal from the NaCl treated ZnO film was observed compared to the control ZnO film. They also observed effects of ion doping in these samples, with the value of $E_F - E_V$ increasing from 3.02 eV to 3.30 eV based on UPS measurements. This result is indicative of stronger n-type doping in the ETL, which improves band alignment and electron transport within the final device, which in turn is expected to enhance the open-circuit voltage (V_{oc}) and depletion region in the device. A slight increase of V_{oc} from 0.554 V to 0.561 V was observed⁸⁰.

Woo et al. demonstrated that ZnO NP passivation can also be achieved through improved annealing procedures, without the need to introduce foreign ions into the ZnO lattice⁸¹. Their method involved heating a small volume of the ZnO solution in a vial for 15 minutes at 80°C. Woo et al. propose a reaction scheme in which the oxygen vacancies of the ZnO lattice react with free OH⁻ groups in the solution to form defect-free ZnO sites and water. Similar to the salt-based method described by Wei et al., this colloidal annealing method is able to more efficiently passivate the ZnO NPs due to the increased availability of the NP surface to the oxygen-containing hydroxyl groups. Woo et al. found that the density of oxygen vacancies was reduced from 20.6 atomic percent (at%) for the annealed sample to 13 at% and 12 at% for the film-phase annealed and colloidal-phase annealed samples, respectively. They also observed reduced PL intensity for the colloidal-phase annealed sample compared to the traditional film-phase annealed sample, further indicating that this method successfully passivated traps and reduced recombination in the ZnO NP film. This colloidal annealing method also induced favorable shifts to the band structure of the ZnO NPs. Woo et al. reported that the strong electronegativity of the oxygen added to the lattice during annealing led to downward shifts of both the conduction and valence bands with a minimal shift of the Fermi level (0.01 eV increase), leading to stronger n-type doping. These shifts are expected to be highly beneficial for charge extraction in the device. Devices fabricated with colloidal-phase annealed ZnO ETLs showed significantly enhanced performance compared to film-phase annealing, with an absolute increase in PCE from 8.76% (film-phase-annealed) to 9.29% (colloidal-phase-annealed). This result was accompanied by an enhanced built-in voltage and depletion region width for the colloidal-phase-annealed sample.

Fang et al. recently developed a method to passivate ZnO NPs by introducing open-shell donor-acceptor organic semiconductors (diradicals) into the ZnO solutions⁸³. Importantly, these molecules contain two unpaired electrons which can be transferred to the ZnO, efficiently passivating the ZnO trap states. This electron transfer is facilitated by the type-II band alignment which exists between the ZnO NPs and the diradical molecules. This

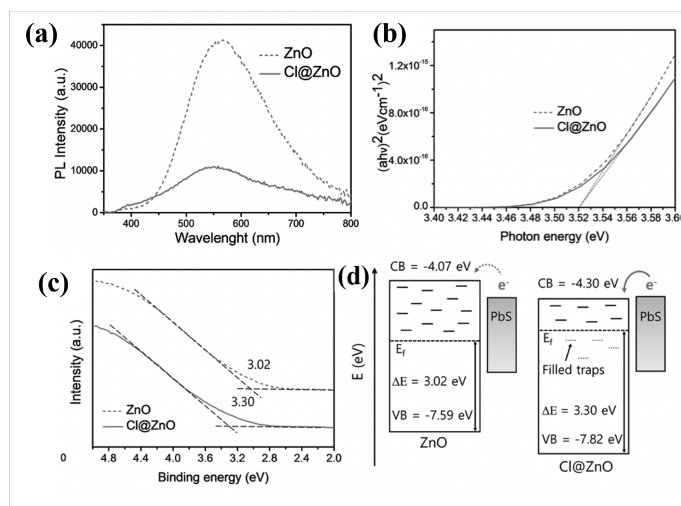


Fig. 4 a) PL spectra, b) Tauc plot, c) UPS spectra of ZnO with (solid) and without (dashed) Cl passivation. d) Schematic band diagram of ZnO without (left) and with (right) Cl derived from optical and UPS analysis. (a-d) Reproduced with permission from Ref. ⁴³ Copyright 2017, Wiley Online Library.

alignment also facilitates hole extraction from ZnO trap states to the diradical molecule, further reducing trap-assisted recombination⁸³. A hybrid ETL is formed by adding the diradical molecule TPAOMe-C8 to the ZnO NP solution before depositing the ETL film. Using this approach, the average PCE was increased from 12.52% in the control device to 13.30% in the hybrid ETL device. Using PL spectroscopy, a significant reduction in trap states in the hybrid ETL was demonstrated, indicating successful passivation of oxygen vacancies. Transient PL measurements were used to study both the fast and slow decay time scales in the deep defect region. The fast decay time decreased from 6.25 ns in the control to 0.75 ns in the TPAOMe-C8. Fang et al. attribute this to hole extraction from the oxygen vacancy defect level into the TPAOMe-C8. They also observed a decrease in the slow decay time, which they attribute to reduced emission from the defect level. This indicates that the diradical molecules successfully reduced radiative recombination through the combination of enhanced electron injection into the ZnO and hole extraction from ZnO defect levels into the diradical molecules. The conductivity of the ZnO films was also tested by making electron-only devices. The results show that the conductivity increases, both in the dark and under illumination, upon the addition of the diradical molecules into the ZnO NP film, which improves the extraction of electrons from the PbS CQD film into the ETL. This result occurs due to the injection of the free electrons from the diradical molecule into the ZnO film. UPS measurements indicated an upward shift of the conduction and valence bands as well as the Fermi level of the ZnO film, resulting in better band alignment with the PbS CQD film.

3.3 ZnO Doping

Many dopants have been utilized to improve the performance of ZnO ETLs including gallium⁸⁴, magnesium^{42,47,85}, aluminum⁸⁶, potassium⁸⁷, and cesium⁸². Generally, dopants have been introduced to increase the ZnO bandgap and enable better band

alignment with the CQD films. Bashir et al. chose indium (In^{3+}), aluminum (Al^{3+}) and gallium (Ga^{3+}) to test as dopants in ZnO to broaden its bandgap and improve transport properties.⁵⁴ With In^{3+} as a ZnO dopant (creating IZO), they were able to improve PCEs by 18%, from 9.4% to 11.1%. Using Tauc plots (Figure 5a), they found that with In^{3+} doping, the ZnO bandgap increased from 3.56 eV to 3.74 eV for IZO, which was the largest bandgap observed. Using UPS (Figure 5b-e), they were able to calculate band energies (Figure 5f), and concluded that IZO had a more favorable band alignment for their PbS CQD absorbing layer, which led to improved device performance. As a result of the improved band alignment, devices made with IZO exhibited a barrier-free interface which simultaneously enabled faster electron injection and more efficient hole blocking characteristics. X-ray photoelectron spectroscopy (XPS) results also show a reduced concentration of surface hydroxyl groups for IZO, which is beneficial for reducing the defect density in the IZO films. PL results agree with this finding. The PL intensity is notably smaller for IZO films compared to ZnO films.

Magnesium is also a popular dopant for ZnO ETLs. Mg can increase the bandgap of ZnO through direct substitution of Mg for Zn in the ZnO lattice⁴². Zhang et al. demonstrated the benefit of this approach by researching the applications of magnesium-doped ZnO (MgZnO) in flexible PbS CQD solar cells⁴². Using MgZnO, they improved the average PCE from 9.2% in their rigid control device to 10.4% in their rigid MgZnO ETL device and 9.4% in a flexible MgZnO ETL device⁴². Zhang et al. first confirmed the incorporation of Mg into the ZnO using XPS. They also observed a slight (≈ 0.15 eV) increase in the ZnO conduction band minimum, leading to improved band alignment with the PbS CQD absorbing layer. Utilizing simulations, they demonstrated that the observed shift in the conduction band minimum and the bandgap of the MgZnO lead to smoother band alignment at the ETL/CQD interface in a PbS CQD solar cell. They confirmed these results experimentally. Based on the current density-voltage (J-V) curves, they found a reduced series resistance of $5.0 \Omega/\text{cm}^2$ compared to $7.4 \Omega/\text{cm}^2$ for the control ZnO film. This result indicates that the MgZnO ETL provides better electron extraction and hole blocking compared to a ZnO ETL, enhancing overall performance. A reduced PL intensity was observed when utilizing a MgZnO ETL, indicating that using the MgZnO film resulted in reduced radiative recombination at the ETL/CQD interface. Transient Voc decay measurements showed that the MgZnO based devices had longer electron lifetimes than the corresponding ZnO devices, meaning that the MgZnO devices exhibit slower recombination rates than ZnO devices, which is highly beneficial for solar cell performance. Similarly, time resolved PL decay measurements revealed that the electron injection times were 0.74 and 0.58 ns for a ZnO ETL and MgZnO ET, respectively. The faster electron injection time implies more ideal band alignment at the ETL/CQD interface, in agreement with the simulation results.

Recently, Choi et al. introduced a doping method based on an azide ion solution to remove unwanted impurities, enhance carrier lifetime and mobility, and provide a more optimal band structure for integration into PbS CQD optoelectronics⁸⁸. Choi et al. found that in addition to surface defects, current ZnO NP

synthesis methods suffer from the strong attraction of the acetate ions from the ZnAc precursor to the ZnO NP surfaces. The acetate groups on the ZnO surfaces hinder charge transport in the ZnO ETL. To overcome this issue, Choi et al. developed an approach to soak the ZnO NP films in a sodium-azide (NaN_3) solution. They then demonstrated using Fourier transform infrared (FTIR) spectroscopy that the azide treated films showed a reduced COO^- peak and an enhanced N_3^- peak, indicating the azide ions successfully exchanged with the acetate ions on the ZnO NP surface. XPS was used to quantify the concentration of oxygen in the lattice (O_L), absorbed oxygen (O_A), and oxygen vacancies (O_V). The reported $\text{O}_L:\text{O}_V:\text{O}_A$ ratios were 60.1:24.4:15.5 and 68.6:21.3:10.1⁸⁸, showing that the azide treatment reduced both vacancies and absorbed oxygen while providing an increased concentration of occupied lattice oxygen sites. This is expected to be very useful for device applications as it will reduce trap-assisted recombination and improve overall charge transport in the device. Indeed, lower defect emission was observed by PL spectroscopy for the azide treated ZnO films. Carrier lifetime was also estimated to have improved from 11.8 ns to 13.2 ns⁸⁸. Based on space-charge limited current measurements, the trap state densities were calculated to be $9.7 \times 10^{15} \text{ cm}^{-3}$ and $7.9 \times 10^{15} \text{ cm}^{-3}$ for the control and azide treated ZnO films, respectively. The azide treatment also provided significant n-type doping, with the value of E_C-E_F decreasing from 0.42 eV to 0.18 eV. This band shifting provides more ideal band alignment with PbS CQD thin films.

4 Experimental Demonstration

Prior work on ZnO ETLs has illustrated the importance of a wide range of synthesis parameters on the PCE and yield of PbS CQD solar cells. These parameters include the heating time, the presence and identity of additives in the ZnO NP solution, and the composition of the dispersion solvent^{56 64 63 35 57 58}. In order to highlight the interaction between these different approaches, we conducted experiments employing each method discussed above while maintaining a common base procedure. Due to its widespread use in literature, we employed the method popularized by Chuang et al. as the basis for further exploration of the correlation between ZnO ETL quality and PbS CQD solar cell yield⁵⁶. By keeping a consistent baseline between experiments, the results presented here are intended to demonstrate the optimal combination of these approaches which simultaneously improves PCE and device yields.

We first varied the heating time of the ZnO synthesis (Fig. 1(a)) from 2 hours and 20 minutes to 3 hours in 10 minute intervals. This range was chosen to cover the heating times commonly found in literature^{24 26 45}. The procedure used for synthesizing the ZnO NPs is illustrated in Fig. 1(a). The procedure is as follows: First, 2.95 grams of zinc acetate dihydrate (ZnAc) are added into 125 mL of methanol. Next, the solution is heated to 58°C and stirred at 1,000 rotations per minute (rpm) until the ZnAc is fully dissolved. Separately, 1.48 g of potassium hydroxide (KOH) is dissolved in 65 mL of methanol. Mild heating (up to 80°C) and stirring (at 300 rpm) were used to dissolve the KOH. Next, the KOH solution is slowly added into the ZnAc solution over the course of 10 minutes. After this is complete, the solution

is maintained at 58°C and 1,000 rpm for the desired heating time. Once the ZnO NPs are formed, the solution is allowed to cool for 1-2 hours prior to being centrifuged at 3,200 rpm for 1 minute. After centrifuging, the methanol is discarded and replaced with fresh solvent, and the washing process is repeated for a total of three iterations. On the final wash, the samples are centrifuged for 5 minutes at 4,000 rpm. Finally, the ZnO NPs are dispersed in chloroform at 30 mg/mL.

Once we had synthesized ZnO NPs with each of the desired heating times, we made devices incorporating ZnO from each trial into devices using the following methods. First, the ZnO solution was deposited onto clean fluorine-doped tin oxide (FTO) substrates by spin casting three layers at 2,000 rpm. The ZnO NP ETLs were then annealed at 200°C for 40 minutes in air. The absorbing layer was prepared based on literature methods involving a solution-phase ligand exchange of lead halides and ammonium acetate¹⁵. The absorbing layer was then annealed at 70°C for 10 minutes in a nitrogen environment. The HTL was prepared using a layer-by-layer solid state ligand exchange, as per standard procedures¹⁵. Finally, 100 nm of gold was thermally evaporated to act as the top contact of the device.

The results for the heating time experiment are shown in Figure 6(b)⁸⁹. The 2 hours and 20 minutes synthesis time resulted in the highest average PCE, but we observed that the resulting NPs were difficult to precipitate. Although the 2 hour and 20 minute heating time yielded an average PCE that was about 0.2% higher than the 2 hour 40 minute heating time, we found that the NPs produced with longer heating times were more easily redispersed, leading to more reliable results and higher device yield. Based on this minimal tradeoff between PCE and yield, we found the optimal heating time to be 2 hours and 40 minutes.

Multiple studies have examined the impact of adding methanol to the final dispersion solvent for the ZnO NPs on the PCE of PbS CQD solar cells, so we next performed a study to determine how the final solvent ratio affected device yield^{35 57 58}. This experiment utilized the same strategies as the heating time experiments described above with a fixed heating time of 2 hours and 40 minutes. The variation for this experiment occurred in the final step, where instead of dispersing the ZnO NPs at 30 mg/mL in pure chloroform, the NPs were dispersed at a fixed concentration of 30 mg/mL, but with varied ratios of CF:MeOH. We found that both the 1:0 ratio and the 1:1 CF:MeOH ratios produced high PCE devices, consistent with literature. We also observed a significant difference in device yield between the two, with the 1:1 ratio outperforming the 1:0 ratio in this regard, as summarized in Figure 6a⁸⁹. Due to the reliability of the 1:1 ratio we found it to be the ideal final solvent ratio for the ZnO synthesis procedure.

We also investigated the effects of the popular additive ethanolamine (MEA). We started by adding MEA to ZnO in chloroform. We tested multiple MEA concentrations of MEA in the chloroform-only ZnO NP solutions and found the optimal MEA concentration to be 0.2 percent by volume. The addition of MEA resulted in a clearer solution, whereas the ZnO solution without MEA was more opaque and agglomeration was clearly visible, as shown in Figure 7b. We performed SEM on ZnO thin films with and without the addition of MEA and saw the same

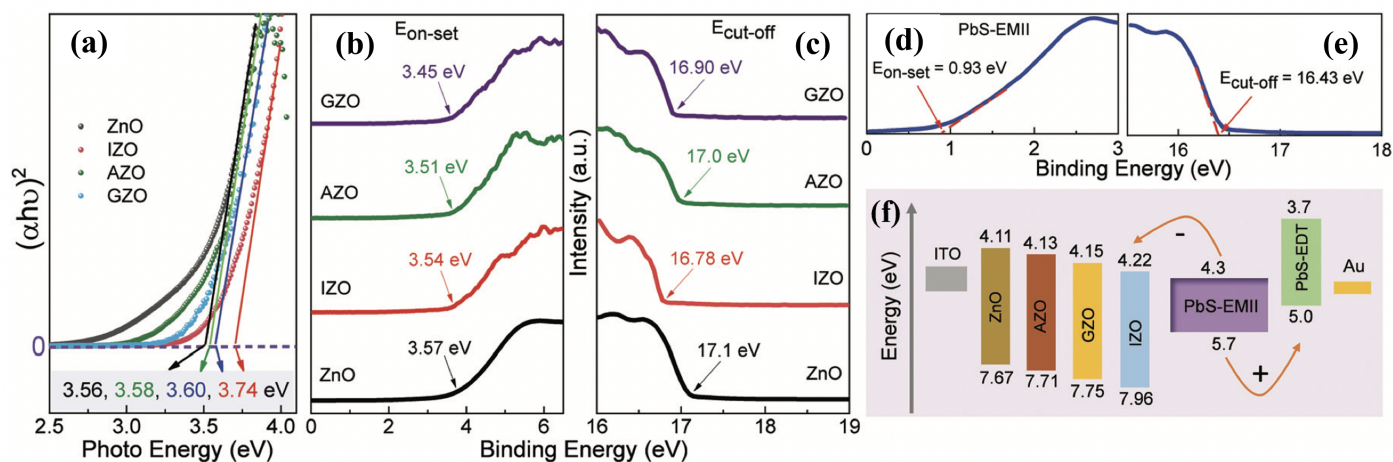


Fig. 5 a) Tauc plot, b), c) UPS of ZnO doped with In^{3+} , Al^{3+} , and Ga^{3+} . d), e) UPS spectra of a PbS CQD based absorbing layer. f) Energy band diagram of ZnO, AZO, GZO, and IZO alignment within a PbS CQD solar cell. (a-f) Reproduced with permission from Ref.⁵⁴ Copyright 2021, Royal Society of Chemistry.

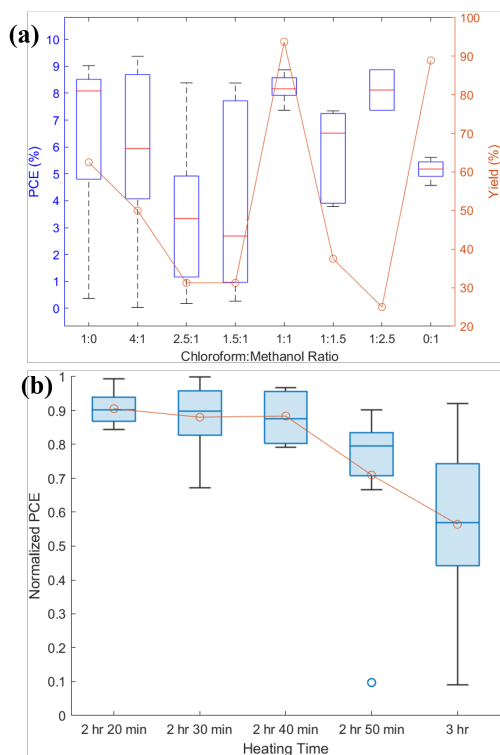


Fig. 6 (a) PCE (blue plot, left y-axis) and yield (orange plot, right y-axis) as a function of the ratio of chloroform and methanol used to disperse the ZnO NP solution. Each ratio contains data for between 9 and 16 devices. (b) Normalized PCE of PbS CQD solar cells prepared with ZnO NPs heated for different amounts of time. 9 devices were tested for each heating time.

trends observed in literature, where the addition of MEA resulted in smoother films with less cracking (Figure 7c-d)^{64 63}. Due to the higher film quality resulting from the addition of MEA, we were able to achieve an increase in PCE from 7.8% to 9.1% (Figure 7a), when comparing the best performing solar cells. This increase was mostly attributable to a higher J_{sc} , which increased from 23.1 mA/cm^2 to 26.5 mA/cm^2 , as well as an increase in FF from 0.58 to 0.60. There was a slight decrease of V_{oc} from 0.58 V to 0.56 V when comparing the best performing solar cells without MEA added to with MEA. We also found that the addition of MEA improved device yields by 10%. This was likely due to the resulting smoother surfaces with less crack formation in the ETL films, leading to less shorting in the full devices. However, adding MEA to our 1:1 CF:MeOH ZnO solution decreased the PCE, resulting in a PCE of 7.2%.

To summarize the experimental findings, the optimal combination of PCE and yield was achieved by heating the ZnO for 2 hours and 40 minutes, washing the nanoparticles in methanol three times, then redispersing the nanoparticles in a 1:1 ratio of chloroform and methanol. We additionally found that switching from pure chloroform to 1:1 CF:MeOH produced more significant PCE improvements than the addition of MEA, so we did not include MEA in our optimized ZnO recipe.

5 Conclusions

In summary, we have presented a comprehensive review of the ZnO recipes used for the ETLs in high performance PbS CQD solar cells over the past several years to understand how these factors affect the PCE. To further enhance our understanding of how these parameters effect overall performance, we have presented a set of experimental studies to highlight their effects on the yield of working devices.

We found that a critical factor for high yield and high performance CQD solar cells was the dispersion solvent. Pure CF and a CF:MeOH ratio of 1:1 were the most prevalent final solvent choices for the ZnO nanoparticle ETL among previously-reported

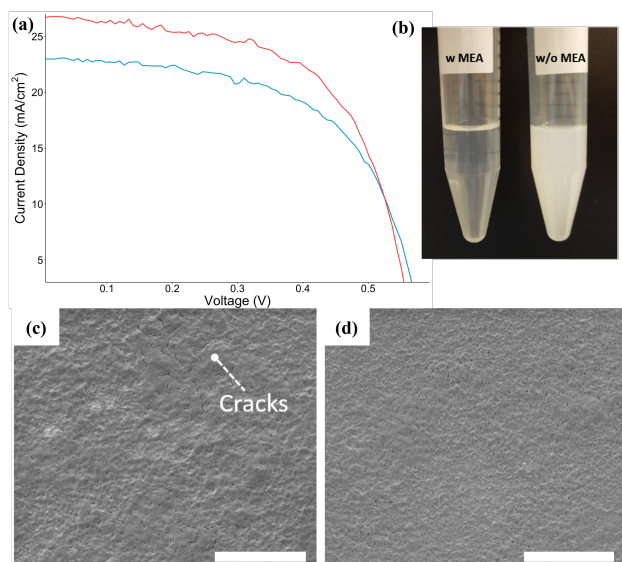


Fig. 7 a) Representative JV curve for a PbS CQD solar cell with (red) and without MEA (blue) as an additive in the ZnO ETL. b) Photographs of a clear ZnO solution with the addition of MEA (left) and a cloudy ZnO solution without MEA (right). c-d) SEM images of ZnO films without MEA (c) and with MEA (d). The scale bars are 10 μm

high performing PbS CQD solar cells. We found that although both choices lead to high performance, a CF:MeOH ratio of 1:1 achieved the highest device yield. We also studied the effect of a common additive, MEA, used for solution stabilization and found that it produced smoother ZnO films with consequently higher CQD solar cell PCEs from ZnO-in-chloroform dispersions. We also analyzed recent work on the ZnO ETL which addressed the issues of surface passivation and band alignment within the full devices. Although there have been many demonstrations of methods to decrease surface defect densities and improve band alignment, none of these techniques have been widely adopted yet. As the field of PbS CQD solar cells matures, simultaneously achieving high PCE and high device yields will be a critical factor in commercializing this technology for use in next-generation applications such as multi-junction solar cells, color-tuned and transparent platforms, and flexible, wearable devices.

Author contributions

Conceptualization: Arlene Chiu and Chengchangfeng Lu; Data Curation: Chengchangfeng Lu and Sreyas Chintapalli; Formal Analysis: Arlene Chiu and Dana Kachman; Funding Acquisition: Susanna Thon; Investigation: Dana Kachman; Methodology: Chengchangfeng Lu and Dana Kachman; Project Administration: Susanna Thon; Resources: Susanna Thon; Software: Yida Lin; Supervision: Susanna Thon; Validation: Daniel Khurgin and Eric Rong; Visualization: Dana Kachman; Writing – Original Draft: Arlene Chiu; Writing – Review & Editing: Arlene Chiu and Dana Kachman

Conflicts of interest

There are no conflicts to declare.

Acknowledgements

This work was supported by the National Science Foundation (DMR-1807342, ECCS-1846239) and the Department of Defense (W911NF2120213). The authors would also like to thank Lulin Li for helpful advice and assistance.

Notes and references

- 1 C. Becker, F. Ruske, T. Sontheimer, B. Gorka, U. Bloeck, S. Gall and B. Rech, *Journal of Applied Physics*, 2009, **106**, 084506.
- 2 I. J. Kramer, J. C. Minor, G. Moreno-Bautista, L. Rollny, P. Kanjanaboos, D. Kopilovic, S. M. Thon, G. H. Carey, K. W. Chou, D. Zhitomirsky, A. Amassian and E. H. Sargent, *Advanced Materials*, 2015, **27**, 116–121.
- 3 A. Loiodice, A. Rizzo, M. Corricelli, M. L. Curri, M. R. Belviso, P. D. Cozzoli, G. Grancini, A. Petrozza and G. Gigli, *Thin Solid Films*, 2014, **560**, 44–48.
- 4 J. He, M. Luo, L. Hu, Y. Zhou, S. Jiang, H. Song, R. Ye, J. Chen, L. Gao and J. Tang, *J. Alloys Compd.*, 2014, **596**, 73.
- 5 I. J. Kramer, G. Moreno-Bautista, J. C. Minor, D. Kopilovic and E. H. Sargent, *Appl. Phys. Lett.*, 2014, **105**, 163902.
- 6 M. Hines and G. Scholes, *Advanced Materials*, 2003, **15**, 1844–1849.
- 7 M. G. Bawendi, M. L. Steigerwald and L. E. Brus, *Annu. Rev. Phys. Chem.*, 1990, **41**, 477.
- 8 J. H. Song and S. Jeong, *Nano Converg.*, 2017, **4**, 21.
- 9 Y. Shirasaki, G. J. Supran, M. G. Bawendi and V. Bulović, *Nat. Photonics*, 2013, **7**, 13.
- 10 Z. Yang, M. Gao, W. Wu, X. Yang, X. W. Sun, J. Zhang, H.-C. Wang, R.-S. Liu, C.-Y. Han, H. Yang and W. Li, *Mater. Today*, 2019, **24**, 69.
- 11 Y. Sun, J. H. Seo, C. J. Takacs, J. Seifert and A. J. Heeger, *Advanced Materials*, 2011, **23**, 1679–1683.
- 12 T. Yang, W. Cai, D. Qin, E. Wang, L. Lan, X. Gong, J. Peng and Y. Cao, *The Journal of Physical Chemistry C*, 2010, **114**, 6849–6853.
- 13 S. Schumann, R. Da Campo, B. Illy, A. Cruickshank, M. McLachlan, M. Ryan, D. Riley, D. McComb and T. Jones, *Journal of Materials Chemistry*, 2011, **21**, 2381–2386.
- 14 Z. Liang, Q. Zhang, O. Wiranwetchayan, J. Xi, Z. Yang, K. Park, C. Li and G. Cao, *Advanced Functional Materials*, 2012, **22**, 2194–2201.
- 15 M. Liu, O. Voznyy, R. Sabatini, F. García de Arquer, R. Munir, A. Balawi, X. Lan, F. Fan, G. Walters, A. Kirmani, S. Hoogland, F. Laquai, A. Amassian and E. Sargent, *Nature Materials*, 2017, **16**, 258–263.
- 16 N. V. Dambhare, A. Sharma, C. Mahajan and A. K. Rath, *Energy Technology*, 2022, **10**, 2200455.
- 17 H.-J. Womelsdorf, W. Hoheisel and G. Passing, *Nanoparticle, redispersible zinc oxide gels*, 2004, US Patent 6,710,091.
- 18 R. Bashir, M. K. Bilal, W. Ahmad, A. Bashir, S. U. Asif, H. Liu, J. Xie, A. Ali and W. Hu, *ACS Applied Nano Materials*, 2021, **4**, 8888–8896.
- 19 S. A. McDonald, G. Konstantatos, S. Zhang, P. W. Cyr, E. J. Klem, L. Levina and E. H. Sargent, *Materials for Sustainable*

- Energy: A Collection of Peer-Reviewed Research and Review Articles from Nature Publishing Group*, World Scientific, 2011, pp. 70–74.
- 20 E. J. Klem, D. D. MacNeil, P. W. Cyr, L. Levina and E. H. Sargent, *Applied physics letters*, 2007, **90**, 183113.
 - 21 N. Zhao, T. P. Osedach, L.-Y. Chang, S. M. Geyer, D. Wanger, M. T. Binda, A. C. Arango, M. G. Bawendi and V. Bulovic, *ACS nano*, 2010, **4**, 3743–3752.
 - 22 J. Huang, Z. Yin and Q. Zheng, *Energy & Environmental Science*, 2011, **4**, 3861–3877.
 - 23 Q. Zhang, C. S. Dandeneau, X. Zhou and G. Cao, *Advanced materials*, 2009, **21**, 4087–4108.
 - 24 J. M. Luther, J. Gao, M. T. Lloyd, O. E. Semonin, M. C. Beard and A. J. Nozik, *Advanced materials*, 2010, **22**, 3704–3707.
 - 25 R. Debnath, M. T. Greiner, I. J. Kramer, A. Fischer, J. Tang, D. A. R. Barkhouse, X. Wang, L. Levina, Z.-H. Lu and E. H. Sargent, *Applied Physics Letters*, 2010, **97**, 023109.
 - 26 C.-H. M. Chuang, P. R. Brown, V. Bulović and M. G. Bawendi, *Nat. Mater.*, 2014, **13**, 796.
 - 27 J. Gao, C. L. Perkins, J. M. Luther, M. C. Hanna, H.-Y. Chen, O. E. Semonin, A. J. Nozik, R. J. Ellingson and M. C. Beard, *Nano letters*, 2011, **11**, 3263–3266.
 - 28 M. Tokumoto, S. H. Pulcinelli, C. V. Santilli and A. Craievich, *Journal of non-crystalline solids*, 1999, **247**, 176–182.
 - 29 W. J. Beek, M. M. Wienk, M. Kemerink, X. Yang and R. A. Janssen, *The Journal of Physical Chemistry B*, 2005, **109**, 9505–9516.
 - 30 S. Mukherjee, S. Pramanik, S. Das, S. Chakraborty, S. Mondal, T. Ghosh, R. Nath and P. K. Kuri, *New Journal of Chemistry*, 2021, **45**, 17009–17024.
 - 31 L. Znaidi, *Materials Science and Engineering: B*, 2010, **174**, 18–30.
 - 32 S.-W. Baek, S. Jun, B. Kim, A. H. Proppe, O. Ouellette, O. Voznyy, C. Kim, J. Kim, G. Walters, J. H. Song *et al.*, *Nature Energy*, 2019, **4**, 969–976.
 - 33 R. Azmi, H. Aqoma, W. T. Hadmojo, J.-M. Yun, S. Yoon, K. Kim, Y. R. Do, S.-H. Oh and S.-Y. Jang, *Advanced Energy Materials*, 2016, **6**, 1502146.
 - 34 Y. Cao, A. Stavrinadis, T. Lasanta, D. So and G. Konstantatos, *Nature Energy*, 2016, **1**, 1–6.
 - 35 X. Lan, O. Voznyy, A. Kiani, F. P. García de Arquer, A. S. Abbas, G.-H. Kim, M. Liu, Z. Yang, G. Walters, J. Xu *et al.*, *Advanced Materials*, 2016, **28**, 299–304.
 - 36 R. Azmi, S.-H. Oh and S.-Y. Jang, *ACS Energy Letters*, 2016, **1**, 100–106.
 - 37 X. Lan, O. Voznyy, F. P. García de Arquer, M. Liu, J. Xu, A. H. Proppe, G. Walters, F. Fan, H. Tan, M. Liu *et al.*, *Nano letters*, 2016, **16**, 4630–4634.
 - 38 Z. Jin, M. Yuan, H. Li, H. Yang, Q. Zhou, H. Liu, X. Lan, M. Liu, J. Wang, E. H. Sargent *et al.*, *Advanced functional materials*, 2016, **26**, 5284–5289.
 - 39 M. Liu, O. Voznyy, R. Sabatini, F. P. García de Arquer, R. Munir, A. H. Balawi, X. Lan, F. Fan, G. Walters, A. R. Kirmani *et al.*, *Nature materials*, 2017, **16**, 258–263.
 - 40 A. Stavrinadis, S. Pradhan, P. Papagiorgis, G. Itskos and G. Konstantatos, *ACS energy letters*, 2017, **2**, 739–744.
 - 41 Z. Yang, J. Z. Fan, A. H. Proppe, F. Arquer, D. Rossouw, O. Voznyy, X. Lan, M. Liu, G. Walters, R. Quintero-Bermudez *et al.*, *Nature communications*, 2017, **8**, 1–9.
 - 42 X. Zhang, P. K. Santra, L. Tian, M. B. Johansson, H. Rensmo and E. M. Johansson, *ACS nano*, 2017, **11**, 8478–8487.
 - 43 J. Choi, Y. Kim, J. W. Jo, J. Kim, B. Sun, G. Walters, F. P. García de Arquer, R. Quintero-Bermudez, Y. Li, C. S. Tan *et al.*, *Advanced Materials*, 2017, **29**, 1702350.
 - 44 A. R. Kirmani, A. D. Sheikh, M. R. Niazi, M. A. Haque, M. Liu, F. P. G. de Arquer, J. Xu, B. Sun, O. Voznyy, N. Gasparini *et al.*, *Advanced Materials*, 2018, **30**, 1801661.
 - 45 Y. Wang, K. Lu, L. Han, Z. Liu, G. Shi, H. Fang, S. Chen, T. Wu, F. Yang, M. Gu *et al.*, *Advanced Materials*, 2018, **30**, 1704871.
 - 46 K. Lu, Y. Wang, Z. Liu, L. Han, G. Shi, H. Fang, J. Chen, X. Ye, S. Chen, F. Yang *et al.*, *Advanced Materials*, 2018, **30**, 1707572.
 - 47 C. Ding, Y. Zhang, F. Liu, Y. Kitabatake, S. Hayase, T. Toyoda, R. Wang, K. Yoshino, T. Minemoto and Q. Shen, *Nanoscale Horizons*, 2018, **3**, 417–429.
 - 48 M. Gu, Y. Wang, F. Yang, K. Lu, Y. Xue, T. Wu, H. Fang, S. Zhou, Y. Zhang, X. Ling *et al.*, *Journal of Materials Chemistry A*, 2019, **7**, 15951–15959.
 - 49 J. Xu, O. Voznyy, M. Liu, A. R. Kirmani, G. Walters, R. Munir, M. Abdelsamie, A. H. Proppe, A. Sarkar, F. P. García de Arquer *et al.*, *Nature nanotechnology*, 2018, **13**, 456–462.
 - 50 C. Ding, F. Liu, Y. Zhang, S. Hayase, T. Masuda, R. Wang, Y. Zhou, Y. Yao, Z. Zou and Q. Shen, *ACS Energy Letters*, 2020, **5**, 3224–3236.
 - 51 H. I. Kim, J. Lee, M.-J. Choi, S. U. Ryu, K. Choi, S. Lee, S. Hoogland, F. P. G. de Arquer, E. H. Sargent and T. Park, *Advanced Energy Materials*, 2020, **10**, 2002084.
 - 52 M.-J. Choi, F. P. García de Arquer, A. H. Proppe, A. Seifitokaldani, J. Choi, J. Kim, S.-W. Baek, M. Liu, B. Sun, M. Biondi *et al.*, *Nature communications*, 2020, **11**, 1–9.
 - 53 H. I. Kim, S.-W. Baek, H. J. Cheon, S. U. Ryu, S. Lee, M.-J. Choi, K. Choi, M. Biondi, S. Hoogland, F. G. de Arquer *et al.*, *Advanced Materials*, 2020, **32**, 2004985.
 - 54 R. Bashir, M. K. Bilal, A. Bashir, J. Zhao, S. U. Asif, W. Ahmad, J. Xie and W. Hu, *Nanoscale*, 2021, **13**, 12991–12999.
 - 55 J. Yang, M. Kim, S. Lee, J. W. Yoon, S. Shome, K. Bertens, H. Song, S. G. Lim, J. T. Oh, S. Y. Bae *et al.*, *ACS Applied Materials & Interfaces*, 2021, **13**, 36992–37003.
 - 56 C.-H. M. Chuang, P. R. Brown, V. Bulović and M. G. Bawendi, *Nature materials*, 2014, **13**, 796–801.
 - 57 P. Li, T. Jiu, G. Tang, G. Wang, J. Li, X. Li and J. Fang, *ACS applied materials & interfaces*, 2014, **6**, 18172–18179.
 - 58 S. Kumar, R. Upadhyay and B. Pradhan, *Solar Energy*, 2020, **211**, 283–290.
 - 59 P. H. Vajargah, H. Abdizadeh, R. Ebrahimifard and M. Golobostanfard, *Applied Surface Science*, 2013, **285**, 732–743.
 - 60 S. Bandyopadhyay, G. Paul, R. Roy, S. Sen and S. Sen, *Materials Chemistry and Physics*, 2002, **74**, 83–91.

- 61 A. Gómez-Núñez, S. Alonso-Gil, C. López, P. Roura and A. Vilà, *The Journal of Physical Chemistry C*, 2017, **121**, 23839–23846.
- 62 P. Sagar, P. Shishodia and R. Mehra, *Applied surface science*, 2007, **253**, 5419–5424.
- 63 A. TUMBUL, *Süleyman Demirel Üniversitesi Fen Edebiyat Fakültesi Fen Dergisi*, 2019, **14**, 155–164.
- 64 K. Noh, M. Kim, S.-H. Lee, H.-S. Yun, T.-H. Lim, Y. Choi, K.-J. Kim, Y. Jiang, K. Beom, M. Kim *et al.*, *Current Applied Physics*, 2019, **19**, 998–1005.
- 65 A. van Dijken, E. A. Meulenkamp, D. Vanmaekelbergh and A. Meijerink, *The Journal of Physical Chemistry B*, 2000, **104**, 1715–1723.
- 66 Q. Wang, D. Zhang, H. Ma, X. Zhang and X. Zhang, *Applied Surface Science*, 2003, **220**, 12–18.
- 67 X. Wei, B. Man, M. Liu, C. Xue, H. Zhuang and C. Yang, *Physica B: Condensed Matter*, 2007, **388**, 145–152.
- 68 A. Gruzintsev and E. Yakimov, *Inorganic materials*, 2005, **41**, 725–729.
- 69 A. Rastogi, S. Desu, P. Bhattacharya and R. Katiyar, *Journal of electroceramics*, 2004, **13**, 345–352.
- 70 H. S. Kang, J. S. Kang, J. W. Kim and S. Y. Lee, *Journal of Applied Physics*, 2004, **95**, 1246–1250.
- 71 S. Shao, K. Zheng, T. Pullerits and F. Zhang, *ACS Applied Materials & Interfaces*, 2013, **5**, 380–385.
- 72 V. Ischenko, S. Polarz, D. Grote, V. Stavarache, K. Fink and M. Driess, *Advanced functional materials*, 2005, **15**, 1945–1954.
- 73 K. Xu, L. Ke, H. Dou, R. Xu, W. Zhou, Q. Wei, X. Sun, H. Wang, H. Wu, L. Li, J. Xue, B. Chen, T.-C. Weng, L. Zheng, Y. Yu and Z. Ning, *ACS Applied Materials & Interfaces*, 2022, **14**, 14783–14790.
- 74 J. P. C. Baena, L. Steier, W. Tress, M. Saliba, S. Neutzner, T. Matsui, F. Giordano, T. J. Jacobsson, A. R. S. Kandada, S. M. Zakeeruddin *et al.*, *Energy & Environmental Science*, 2015, **8**, 2928–2934.
- 75 J. Choi, S. Song, M. T. Hörantner, H. J. Snaith and T. Park, *ACS nano*, 2016, **10**, 6029–6036.
- 76 I. Robel, M. Kuno and P. V. Kamat, *Journal of the American Chemical Society*, 2007, **129**, 4136–4137.
- 77 G.-H. Kim, F. P. García de Arquer, Y. J. Yoon, X. Lan, M. Liu, O. Voznyy, Z. Yang, F. Fan, A. H. Ip, P. Kanjanaboos *et al.*, *Nano letters*, 2015, **15**, 7691–7696.
- 78 J. Khan, X. Yang, K. Qiao, H. Deng, J. Zhang, Z. Liu, W. Ahmad, J. Zhang, D. Li, H. Liu *et al.*, *Journal of Materials Chemistry A*, 2017, **5**, 17240–17247.
- 79 L. K. Jagadamma, M. Abdelsamie, A. El Labban, E. Aresu, G. O. N. Ndjawa, D. H. Anjum, D. Cha, P. M. Beaujuge and A. Amassian, *Journal of Materials Chemistry A*, 2014, **2**, 13321–13331.
- 80 Y. Wei, M. Xing, D. Wang and R. Wang, *Energy Reports*, 2020, **6**, 2370–2375.
- 81 H. K. Woo, M. S. Kang, T. Park, J. Bang, S. Jeon, W. S. Lee, J. Ahn, G. Cho, D.-K. Ko, Y. Kim, D.-H. Ha and S. J. Oh, *Nanoscale*, 2019, **11**, 17498–17505.
- 82 F. Yang, Y. Xu, M. Gu, S. Zhou, Y. Wang, K. Lu, Z. Liu, X. Ling, Z. Zhu, J. Chen, Z. Wu, Y. Zhang, Y. Xue, F. Li, J. Yuan and W. Ma, *Journal of Materials Chemistry A*, 2018, **6**, 17688–17697.
- 83 S. Fang, J. Huang, R. Tao, Q. Wei, X. Ding, S. Yajima, Z. Chen, W. Zhu, C. Liu, Y. Li, N. Yin, L. Song, Y. Liu, G. Shi, H. Wu, Y. Gao, X. Wen, Q. Chen, Q. Shen, Y. Li, Z. Liu, Y. Li and W. Ma, *Advanced Materials*, 2023, 2212184.
- 84 K.-S. Shin, K.-H. Lee, H. H. Lee, D. Choi and S.-W. Kim, *The Journal of Physical Chemistry C*, 2010, **114**, 15782–15785.
- 85 Y. Gao, R. Patterson, L. Hu, L. Yuan, Z. Zhang, Y. Hu, Z. Chen, Z. L. Teh, G. Conibeer and S. Huang, *Nanotechnology*, 2018, **30**, 085403.
- 86 H. Karaagac, E. Yengel and M. S. Islam, *Journal of alloys and compounds*, 2012, **521**, 155–162.
- 87 R. Azmi, G. Seo, T. K. Ahn and S.-Y. Jang, *ACS Applied Materials & Interfaces*, 2018, **10**, 35244–35249.
- 88 Y. K. Choi, T. H. Kim, B. K. Jung, T. Park, Y. M. Lee, S. Oh, H. J. Choi, J. Park, S.-I. Bae, Y. Lee, J. W. Shim, H. Y. Park and S. J. Oh, *Small*, 2023, 2308375.
- 89 D. Kachman, A. Chiu, D. Gudi, C. Lu, E. Rong, S. Chintapalli, Y. Lin, D. Khurgin, D. Seifu, R. C. Budhani and S. M. Thon, 2023 IEEE 50th Photovoltaic Specialists Conference (PVSC), 2023.